Hierarchically ordered porous superstructure embedded with readily accessible atomic pair sites for enhanced CO_2 electroreduction

Lei Jiao [a,c], Xiaofang Li [a], Wenbo Wei [a], Sheng-Hua Zhou [a], Shu-Guo Han [a], Dong-Dong Ma [a], Yue Mao [a], Qiang Xu [e,f,*], Xin-Tao Wu [a,d], Qi-Long Zhu [a,b,c,d,**]

[a] State Key Laboratory of Structural Chemistry, Fujian Institute of Research on the Structure of Matter, Chinese Academy of Sciences (CAS), Fuzhou 350002, China
[b] Fujian Science & Technology Innovation Laboratory for Optoelectronic Information of China, Fuzhou 350108, China
[c] College of Chemistry and Chemical Engineering, Jiangxi Normal University, Nanchang 330022, China
[d] University of Chinese Academy of Sciences, Beijing 100049, China
[e] Shenzhen Key Laboratory of Micro/Nano-Porous Functional Materials (SKLPM), Department of Chemistry and Department of Materials Science and Engineering, Southern University of Science and Technology (SUSTech), Shenzhen 518055, China
[f] Institute for Integrated Cell-Material Sciences (iCeMS), Kyoto University, Kyoto 606-8501, Japan

ARTICLE INFO

ABSTRACT

Herein, a hierarchically ordered porous superstructure of N-doped carbon embedded with readily accessible Fe-Ni diatomic sites (FeNi DASs/HOPSNC) has been synthesized for highly efficient CO_2 electroreduction. By integrating additional secondary mesopores into the ordered macroporous skeleton, this distinctive superstructure exhibits greatly enhanced accessibility and mass transfer. Benefiting from the unique structure merits including the synergistic effect in Fe-Ni atomic pair sites and the multi-level porosity, such diatomic site catalyst affords an outstanding electrocatalytic performance with excellent activity and selectivity for CO_2-to-CO conversion and remarkable stability. Furthermore, systematic characterizations and density functional theory calculations unveiled that the electronic interaction within the diatomic pairs leads to the optimized electronic state and decreased reaction energy barrier for generating COOH* intermediate and weakening the binding strength of CO*, thereby improving the intrinsic catalytic activity and selectivity. This work may inspire further development of high-performance diatomic site catalysts for CO_2 electroreduction and other electrosynthesis.

1. Introduction

The electrocatalytic reduction of CO_2 using renewable electricity into high value-added chemicals, feedstocks and fuels not only mitigates anthropogenic CO_2 emission but also alleviates our reliance on fossil fuels, which is of great strategic significance to achieve the carbon neutral and sustainable future [1–4]. Importantly, how to design efficient and stable electrocatalysts for CO_2 reduction reaction (CO_2RR) with the large current density is urgent. Numerous electrocatalysts have been extensively explored for CO_2RR, such as metallomacrocycle molecules [5–7], noble metals [8–10], metal atomic site catalysts [11–14], etc. Among them, non-precious metal single-atom catalysts (SACs) have sparked tremendous interest toward various catalytic reactions due to

their ultrahigh atomic utilization, superb activity, selectivity and low manufacturing cost [15–21].

Among these non-precious SACs for CO_2RR, Ni-SAs have been reported to exhibit decent Faradaic efficiency (FE), but require large initial potentials due to sluggish kinetics of the first proton-coupled electron transfer ($CO_2 + H^+ + e^- \rightarrow$ *COOH) [22–25]. On the other hand, Fe-SAs possess the lower initial potentials for CO_2RR; however, the strong binding between iron site and *CO intermediates seriously damages the stability [12,26,27]. In order to promote the formation of *COOH and/or the desorption of *CO during the CO_2RR process, some endeavors has been devoted to tuning the electronic configurations of central metal atoms by creating vacancy or adjusting the coordination environment to improve their catalytic activity [28,29]. Nevertheless,

recent studies have shown that the active metals at the single-atom level are not always favorable for the catalytic process, because the synergies between adjacent metal single atoms (SAs) are weakened with increasing neighbor distance [30–32]. In this regard, constructing the transition metal catalysts with atomic pair structures may harvest more intriguing catalytic properties, which can not only increases the atomic site density but also breaks the stubborn restriction of scaling relations [19,33–36]. Consequently, we speculate that designing Fe-Ni diatomic catalysts (DACs) could utilize the electronic interaction of two adjacent atomic hetero-metal species to achieve their complementary functions and synergies, optimizing adsorption-desorption behaviors of intermediates during CO_2RR. Although several Fe-Ni DACs have been reported, the regulation of the coordination configuration at the atomic levels is still highly expected yet challenging, and the structure-activity relationship needs further investigation to clarify the unpredictable catalytic performance.

In addition to regulating the local electronic structure of the metal centers, the number of available atomic sites and the rate of mass transfer also have important effects on the final activity of metal atomic site catalyst [37,38]. Metal-organic frameworks (MOFs) possessing N-rich organic ligands and tunable porosity have been identified as excellent self-templated precursors for forming atomically dispersed metal-nitrogen (M-N$_x$) sites on carbons [39–42]. However, the porosity of the carbons derived by thermal activation generally exists in the form of inherent and predominant micropores, with only a small amount of mesopores. As a result, most of the metal atomic sites are buried deeply in the carbon matrix and stay inactive, which undoubtedly limits the accessibility of the reactants to the active centers and restricts the mass transfer of molecules and ions during the catalytic process [37,43]. In this perspective, much efforts have been devoted to improve the mass transfer of carbon-based SAC materials, which follows that creating mesoporosity, especially large mesopores (>5 nm), is an effective strategy to afford sufficiently available surface area and enhance the utilization of active sites to improve the catalytic properties [44–46]. To date, various methods, including hard/soft template methods and direct polymerization method, have been employed to synthesize mesoporous materials. Nonetheless, the majority of the pores with a random distribution are isolated from each other, which leads to the restricted mass transfer and diffusion. The blockage of some pores hinder the accessibility of fresh reactants to the active sites, the accumulation of products can lead to catalyst deactivation, resulting in a fraction of the electrochemically dead surfaces [47]. Ordered macroporous structures have been recently introduced to expose more active sites and reduce mass transfer resistance [48–50]. However, these pores are mainly large pores (>50 nm), which results in the limited positive effect. Precise control of the ordering and uniformity of multiscale pores in MOF-derived carbon materials is still challenging, which may largely promote mass diffusion in the catalytic process and the accessibility to the active sites.

Herein, a hierarchically ordered porous superstructure of N-doped carbon embedded with readily accessible Fe-Ni atomic pair sites has been synthesized for highly efficient industrial-level CO_2RR. To our knowledge, this is the first report using ZIF-8 as the precursor to construct the hierarchically ordered porous superstructure embedded with diatomic pairs for CO_2RR. It is found that the hierarchically ordered porous superstructure significantly improves the accessibility of dispersed active diatomic sites and accelerates electrolyte diffusion by reducing and smoothing diffusion paths, leading to an excellent CO_2RR activity. Moreover, the d-orbital energy level of Ni site is shifted toward Fermi energy level by introducing neighbor Fe site, simultaneously decreasing the reaction barrier of the rate-determining step (RDS) and facilitating *COOH adsorption and *CO desorption during the CO_2RR process [51]. Diatomic pair configuration and coordination path of the catalyst were systematically interpreted by aberration-corrected scanning transmission electron microscopy (STEM) and X-ray absorption spectroscopy (XAS). Density functional theory (DFT) calculations show that the reaction barrier of the Ni-Fe diatomic pair sites is significantly

reduced compared to that of the isolated single-atom Fe or Ni sites. Notably, the as-prepared FeNi DASs/HOPSNC catalyst exhibited a high Faradaic efficiency of 94.5%, large current densities up to 300 mA cm^{-2} and remarkable durability, surpassing the single-metal counterparts, Fe SAs/HOPSNC and Ni SAs/HOPSNC. This work provides a guideline for rationally designing both spatial structure and atomic site structure of electrocatalysts for boosting the catalytic properties.

2. Experimental

2.1. Materials synthesis

2.1.1. Preparation of Polystyrene (PS) monolith

Monodisperse PS spheres were prepared according to the reported work [45]. In detail, 100 mL deionized water (18 MΩ cm^{-2}) and 0.5 g PVP were added into a three-necked round-bottom flask (250 mL). The mixture was heated to 70 °C at 600 rpm and purged with nitrogen gas. Then, 13 mL of styrene was added into the above solution, kept at 70 °C for 30 min, followed by the addition of 20 mL of aqueous solution containing 0.3 g $K_2S_2O_8$ as initiator and the reaction was continued for 24 h. The obtained suspension was centrifuged and dried at 60 °C overnight to obtain an ordered PS monolith.

2.1.2. Synthesis of OM-Fe/Ni-ZIF-8 and derived FeNi DASs/HOPSNC

Firstly, 2-methylimidazole (6.75 g) and $Zn(NO_3)_2 \cdot 6\ H_2O$ (8.15 g) were immersed into 45 mL of methanol solution containing 40 mg Fe $(NO_3)_3 \cdot 9\ H_2O$ with stirring. Then the ordered PS template (d ≈ 280 nm) was immersed into the above solution for 30 min, and further treated with a vacuum degassing process for 10 min. Next, this impregnated PS template was transferred to petri dishes and dried at 60 °C for 6 h and then transferred to the mixture solution containing 15 mL methanol and 15 mL $NH_3 \cdot H_2O$ to trigger the formation of ZIFs. After vacuum degassing for 5 min and placing at room temperature and atmospheric pressure for 24 h, Fe-ZIF-8 embedded inside the PS template was formed. The obtained Fe-ZIF-8 @PS was subsequently immersed in DMF to remove the PS. Finally, the ordered macroporous Fe-doped ZIF-8 (OM-Fe-ZIF-8) single-crystals were obtained by further filtration and drying. Further, 100 mg of the as-prepared OM-Fe-ZIF-8 powder was first dispersed into 10 mL of methanol. Afterwards, $Ni(NO_3)_2 \cdot 6\ H_2O$ (100 mg mL^{-1}, 100 μL) was added dropwise at room temperature. The resulting solution was subjected to vigorous stirring for 12 h at room temperature to ensure the ZIF-8 framework sufficiently absorbed the nickel salts. Next, the above mixture was filtrated, followed by drying the powder in a vacuum oven at 60 °C for 12 h, resulting to OM-Fe/Ni-ZIF-8. Finally, 100 mg of as-prepared OM-Fe/Ni-ZIF-8 and 300 mg of dicyandiamide in a porcelain boat were heated to 900 °C under Ar flow for 2 h to yield FeNi DASs/ HOPSNC.

2.1.3. Synthesis of OM-Ni-ZIF-8 and derived Ni SAs/HOPSNC

The synthetic procedure was similar to that of FeNi DASs/HOPSNC. Specially, $Ni(NO_3)_2 \cdot 6\ H_2O$ (100 mg mL^{-1}, 100 μL), $Zn(NO_3)_2 \cdot 6\ H_2O$ (8.15 g) and 2-methylimidazole (6.75 g) was simultaneously added into 45 mL of methanol to prepare OM-Ni-ZIF-8, which was then directly used for pyrolysis to obtain Ni SAs/HOPSNC.

3. Results and discussion

3.1. Synthesis and characterizations of FeNi DASs/HOPSNC

The preparation of the hierarchically ordered porous superstructured FeNi DASs/HOPSNC is schematically illustrated in Fig. 1. Briefly, the pre-synthesized PS with diameter of 280 nm were first assembled into a three-dimensional (3D) and highly ordered PS template (Fig. S1). The methanol precursor solution containing 2-methylimidazole, $Zn(NO_3)_2 \cdot 6\ H_2O$ and $Fe(NO_3)_3 \cdot 9\ H_2O$ was introduced into the voids of 3D ordered PS template by forced impregnation. During the nucleation and growth of
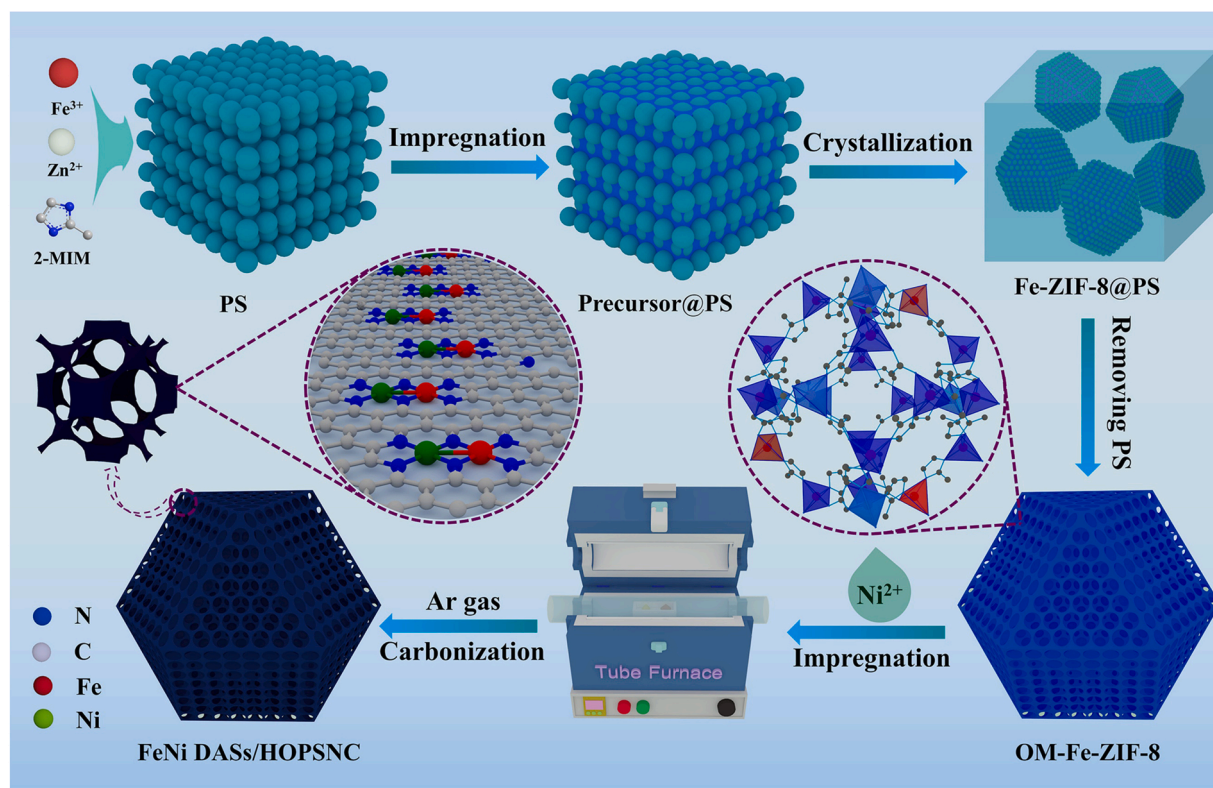
Fig. 1. Schematic illustration of synthesis procedure for FeNi DASs/HOPSNC with the hierarchically ordered porous superstructure.

ZIF-8 in CH_3OH/NH_3OH mixed solution, Fe^{3+} ions can be chemically bonded to 2-methylimidazole ligand, which could be uniformly doped into ZIF-8 nanocrystals instead of being adsorbed physically in the cavity of ZIF-8. Subsequently, the PS template was removed using DMF to obtain the ordered macroporous single-crystals of Fe-doped ZIF-8 (OM-Fe-ZIF-8). The as-obtained OM-Fe-ZIF-8 was then added to the solutions of nickel nitrate at different concentrations, and the nickel ions (1.12 Å) were encapsulated in the small cavities (<5 Å) of OM-Fe-ZIF-8 (Fig. 1). When the resultant OM-Fe/Ni-ZIF-8 as the precursor was subsequently mixed with dicyandiamide (DCDA) and pyrolyzed, DCDA would release plentiful NH_3 gas during its decomposition at 300–350 °C which was uniformly absorbed inside the crystal cavities and channels, thus ensuring the homogeneous etching in the MOF to promote the transformation from micropores to mesopores. Simultaneously, the Fe and Ni ions within ZIF framework could be in situ transformed into the highly dispersed Fe-Ni atomic sites during thermal activation, alleviating their agglomeration. For comparative study, the single-metal counterparts Ni SAs/HOPSNC and Fe SAs/HOPSNC were also constructed through a similar method without Fe or Ni species.

Powder X-ray diffraction (PXRD) patterns show that the OM-Fe/Ni-ZIF-8 precursor has a similar crystal structure to ZIF-8, as shown in Fig. S2a. The PXRD patterns of FeNi DASs/HOPSNC, Fe SAs/HOPSNC and Ni SAs/HOPSNC show two wide diffraction peaks at about 24° and 44° corresponding to the carbon (002) plane and (101) plane, respectively (Fig. S2b). No peaks of metallic phases or metal compounds were observed in all these catalysts, indicating that iron and nickel metals could be highly dispersed at the atomic level.

The morphology features were characterized by scanning electron microscope (SEM). As shown in Figs. 2a,b and S3, the SEM images of OM-Fe/Ni-ZIF-8 indicate the rhombic dodecahedral single-crystal particles of ca. 1.4 μm featuring a 3D interconnected ordered macroporous structure. Upon the pyrolyzation of the mixture of OM-Fe/Ni-ZIF-8 and DCDA at 900 °C for 2 h, the in situ reduced zinc metal with low boiling point (907 °C) was volatilized, while the rhombic dodecahedra

morphology and ordered macroporous structure were well preserved (Figs. 2c, d and S4). Notably, as presented in Fig. 2e, aside from the original ordered macroporous skeleton structure, large quantities of mesopores are homogeneously distributed throughout the carbon walls of FeNi DASs/HOPSNC, forming a hierarchically ordered porous superstructure. The transmission electron microscopy (TEM) image further manifests that such distinctive 3D superstructure consists of highly ordered macropores and mesopores (Fig. 2f). The aberration-corrected high-angle annular dark-field scanning TEM (AC-HADDF-STEM) images of FeNi DASs/HOPSNC illustrate the homogeneously isolated dispersion of Fe and Ni atoms and a large part of the bright spots occurring in pairs (circled by red boxes) over the carbon skeleton with the high metallic density and without clusters and nanoparticles (Fig. 2g,h), which suggests that, in addition to the single-atom metal sites, there could also exist diatomic sites. Furthermore, the distances of the atomic pairs randomly selected were statistically analyzed to be 2.5 Å ± 0.03, uncovering the possible presence of diatomic coordination configuration (Fig. 2i,j). The energy-dispersive X-ray (EDX) spectroscopy confirms the uniform dispersion of Fe, Ni, C, N throughout the FeNi DASs/HOPSNC (Figs. 2k and S5), among which the contents of Fe and Ni were detected by inductively coupled plasma (ICP) to be 0.62 and 1.67 wt%, respectively (Table S1).

As comparison, the SEM and TEM measurements reveal that both single-metal counterparts, Fe SAs/HOPSNC and Ni SAs/HOPSNC, exhibit the similar hierarchically ordered porous superstructure with FeNi DASs/HOPSNC, except for their isolated single-atom Fe and Ni sites (Figs. S6 and S7). In addition, the similar intensity ratios of D-band and G-band (I_D/I_G) in the Raman spectra of the three catalysts suggest their resembling graphitization degree and surface defects (Fig. S8).

To probe the critical role of DCDA in introducing mesopores into the macroporous N-doped carbon skeleton during preparing FeNi DASs/HOPSNC, the porosity of the material series prepared with different mass ratios of DCDA to OM-Fe/Ni-ZIF-8 was studied. The nitrogen sorption isotherms of the materials prepared with DCDA exhibit the
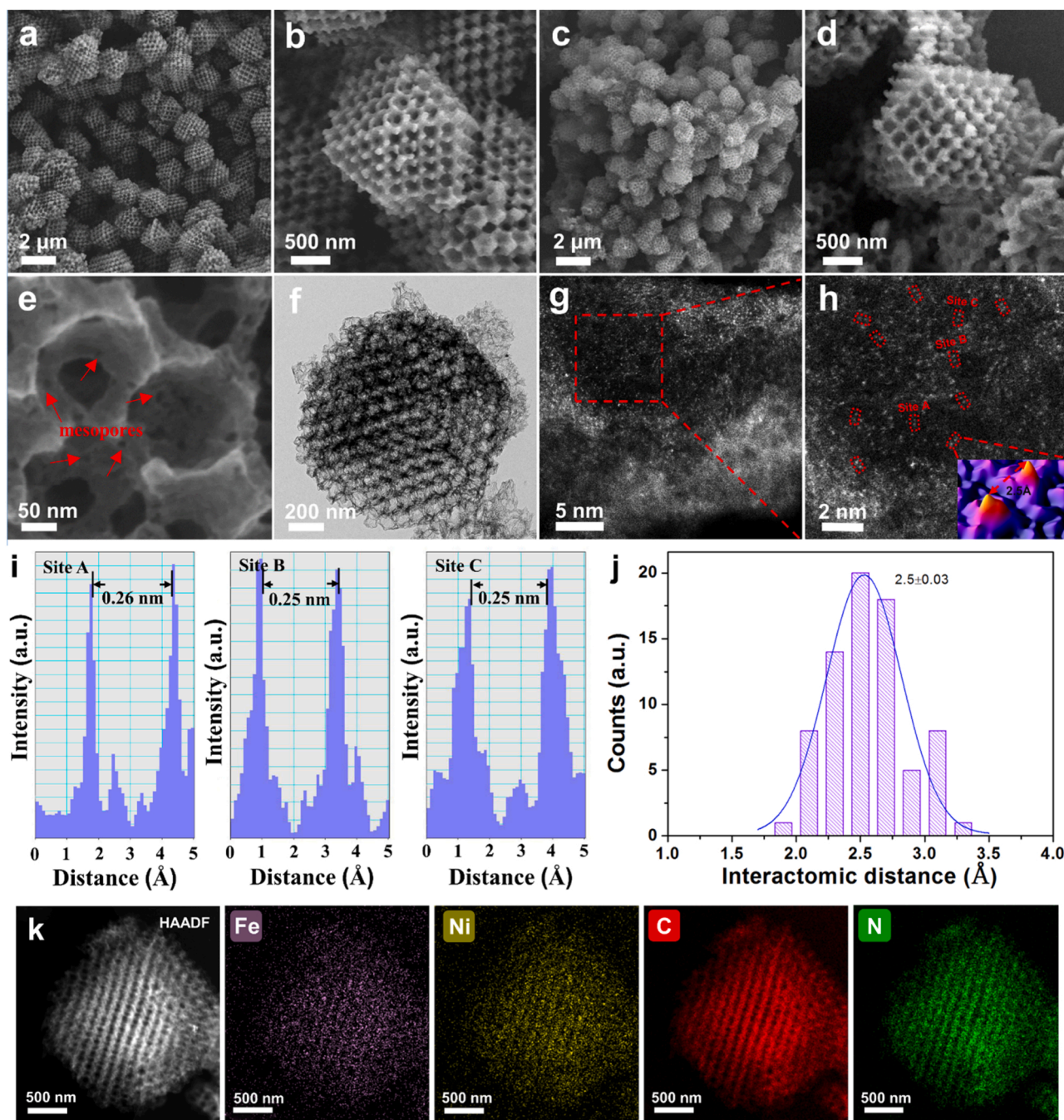
Fig. 2. (a, b) SEM images of OM-Fe/Ni-ZIF-8; (c-e) SEM and (f) TEM images of FeNi DASs/HOPSNC; (g, h) high-resolution AC-HAADF-STEM images of FeNi DASs/ HOPSNC. Inset is 3D atom-overlapping Gaussian-function fitting map; (i) intensity profiles of the three sites indicated in (h); (j) the distance statistics of the atomic pairs in FeNi DASs/HOPSNC; (k) AC-HAADF-STEM and corresponding EDX elemental mapping images of FeNi DASs/HOPSNC.

typical type-IV isotherms with apparent hysteresis loops at a relatively high pressure of $0.8 < p/p_0 < 1.0$, indicating the presence of mesopores (Fig. 3a). By contrary, FeNi DASs/HOPSNC-0 obtained without DCDA presents a type-I isotherm profile and the corresponding tiny amounts of mesopore in size distribution, which indeed confirm a micropore dominated structure. According to the Brunauer-Emmett-Teller (BET) results, with the increase of the DCDA dosage during pyrolysis, though the surface areas of the resultant FeNi DASs/HOPSNC decrease regularly from 828 to 413 m^2 g^{-1}, their volumes of micropores and mesopores significantly increase from 0.75 to 1.67 cm^3 g^{-1} (Fig. 3a). The pore size distributions estimated from the Barrett-Joyner-Halenda (BJH) model clearly show that the materials prepared with DCDA possess affluent mesopores ranging from 2 to 50 nm (Fig. 3b). Furthermore, as visually

presented by SEM in Fig. 3c, in addition to interconnected ordered macropores, abundant homogeneous mesopores are observed on the carbon wall architectures. However, the addition of too much DCDA would lead to the partial collapse of the ordered macroporous skeleton in FeNi DASs/HOPSNC-4. Consequently, FeNi DASs/HOPSNC-3 with plentiful mesopores and maintained ordered superstructure was used as the electrocatalyst for the subsequent investigation. The additional mesopores in FeNi DASs/HOPSNC will not only intensify the exposure of interior active sites but also facilitate mass transport efficiency, and thus be helpful to improve the electrocatalytic performance of CO_2RR.

As shown in Fig. 4a, the valence status and composition of surface elements of FeNi DASs/HOPSNC were further determined by X-ray photoelectron spectroscopy (XPS). According to the Fe 2p and Ni 2p XPS
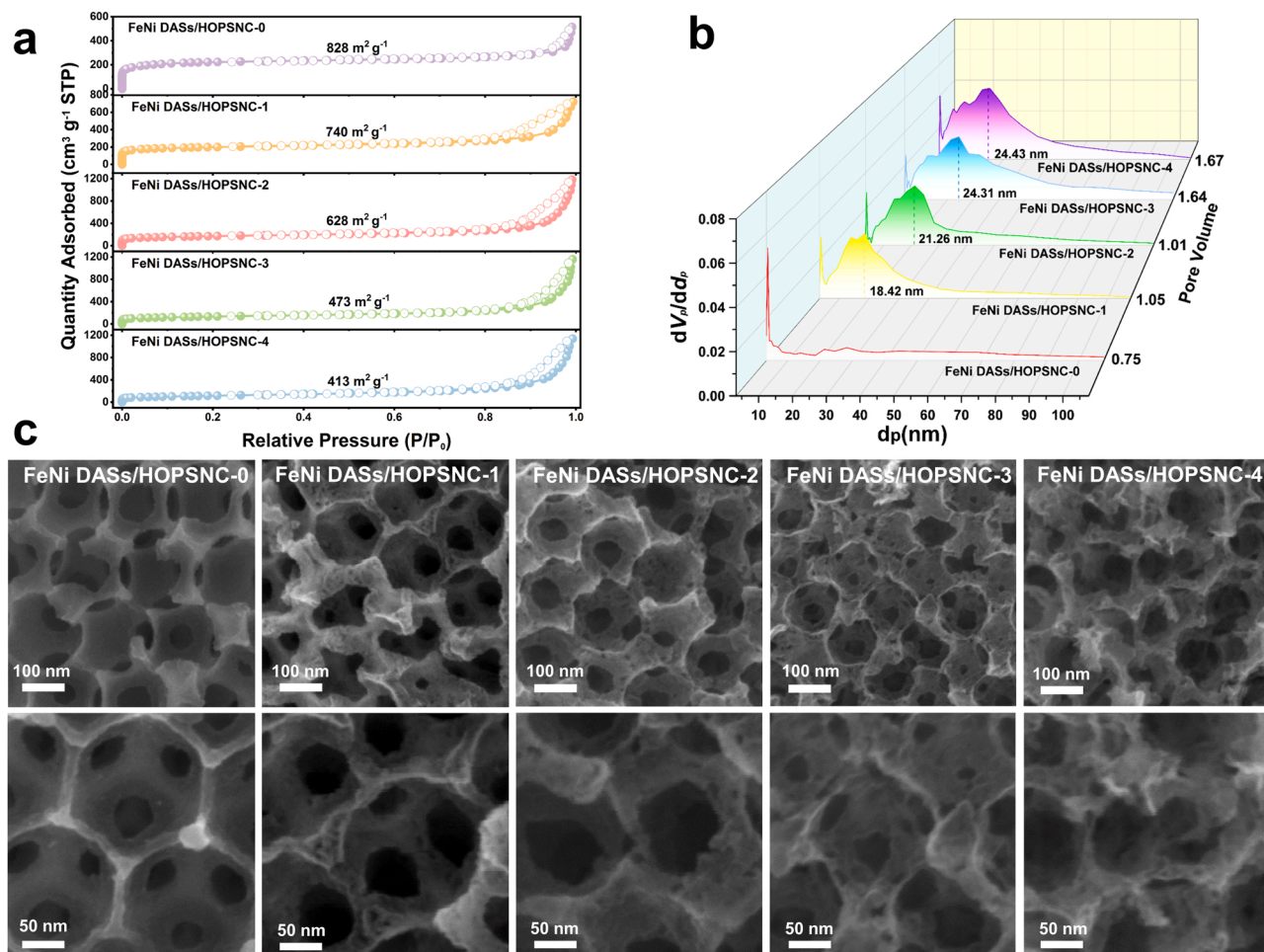
Fig. 3. (a) N$_2$ sorption isotherms; (b) mesopore size distribution curves and pore volumes and (c) SEM images of FeNi DASs/HOPSNC-*X* prepared with the different mass ratios of DCDA to OM-Fe/Ni-ZIF-8.

spectra of FeNi DASs/HOPSNC, the Fe and Ni peaks are shifted towards a lower and a higher binding energy, respectively, as compared to the single-metal counterparts (Fig. S9), indicating the existence of the strong Ni-Fe coupling interaction and partial electron transfer from Ni to Fe atoms. Besides, the absence of Ni^0 and Fe^0 peaks indicates that Ni and Fe exist substantially in the form of single atoms rather than metallic nanoparticles or clusters. The total nitrogen content of FeNi DASs/HOPSNC was tested to be 9.86 at%, higher than that (6.47 at%) of the counterpart prepared without DCDA, and the slight increase in pyridine nitrogen content could be beneficial to stabilize the atomic metal atoms (Fig. S10). Furthermore, the N 1 s spectra of FeNi DASs/HOPSNC, Ni SAs/HOPSNC and Ni SAs/HOPSNC are split into five kinds of nitrogen configurations corresponding to pyridine N (398.5 eV), pyrrole N (401.2 eV), graphite N (402.1 eV), oxidic N (403.6 eV), and metal nitrogen (M-N) in a phthalocyanine-like structure at 399.6 eV. Among these N species, the pyridinic N with higher content in the carbon support is considered as the major anchor sites for single atoms and the increase in M-N peak area followed by an increase in metal content in the materials suggests that the Fe and Ni atoms are atomically dispersed and basically coordinated with N (Fig. S10), rather than forming nanoparticles or clusters, which is consistent with the TEM observation [26,52].

To further investigate the coordination environment and chemical information of the Fe and Ni atoms in catalysts, X-ray absorption near-edge structure (XANES) and extended X-ray fine structure spectroscopy (EXAFS) analysis were conducted. The Fe K-edge XANES spectra of Fe element in FeNi DASs/HOPSNC and Fe SAs/HOPSNC are located

between those of Fe foil and Fe phthalocyanine (Fe Pc), proving that the valence state of the atomic Fe sites is between 0 and + 2 (Fig. 4b). Similarly, as shown in Fig. 4c, the Ni K-edge XANES spectra confirm that the average valence state of the atomic Ni sites is lower than + 2. Meanwhile, the Ni K-edge XANES spectrum of FeNi DASs/HOPSNC shifts towards a higher energy relative to Ni SAs/HOPSNC. On the contrary, FeNi DASs/HOPSNC shows a bit lower adsorption edge than Fe SAs/HOPSNC in the Fe K-edge XANES spectra. These results indicate that the partial electron is transferred from Ni to Fe, in good accordance with XPS results. Furthermore, the intensity of the pre-edge peak at 7114 eV for FeNi DASs/HOPSNC is slightly lower than that of FePc, indicating the D_{4h} symmetric Fe-N$_4$ structure is broken (Fig. 4b). Fig. 4c shows a pre-edge peak at approximately 8334 eV, which marks the hybridization of the 3d and 4p orbitals of the Ni central atom. Compared with Ni SAs/HOPSNC and Ni-Pc, the stronger peak intensity in FeNi DASs/HOPSNC is attributed to the more distorted D_{4h} symmetry, which could be attributed to the electronic interaction and the distorted co-ordination of the Fe-Ni atomic pairs. In addition, in the Fourier trans-formed (FT)-EXAFS spectra of Fe K-edge (Fig. 4d), the predominant peaks for FeNi DASs/HOPSNC and Fe SAs/HOPSNC at 1.53 Å originate from the scattering of first shell Fe-N path, corresponding to the Fe-N first shell coordination. Notably, FeNi DASs/HOPSNC has a distinct metallic path at 2.06 Å in the FT-EXAFS at both Ni and Fe K-edge, which is not found in those of the single-metal Fe SAs/HOPSNC and Ni SAs/HOPSNC, confirming the formation of diatomic coordination configu-ration. The EXAFS curve-fitting analysis of Ni K-edge and Fe K-edge for FeNi DASs/HOPSNC reveals that Fe-Ni interaction path fits well with the
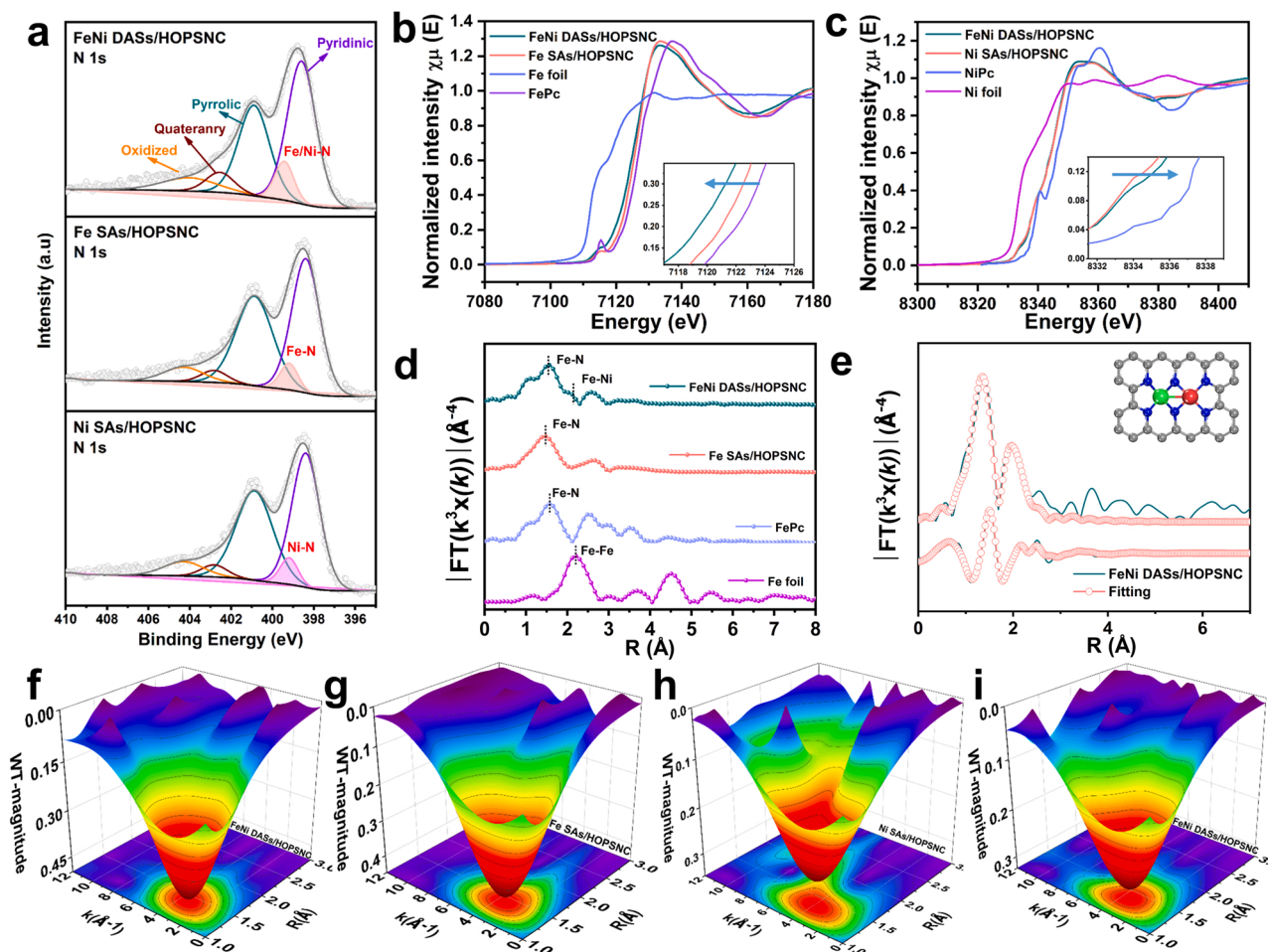
Fig. 4. (a) High-resolution N 1s spectra; (b) Fe K-edge and (c) Ni K-edge XANES spectra (the insets show the enlarged pre-edge region); (d) FT-EXAFS spectra of Fe K-edge; (e) FT-EXAFS fitting curves of Ni K-edge for FeNi DASs/HOPSNC in R space; WT-EXAFS plots of Fe K-edge EXAFS for (f) FeNi DASs/HOPSNC and (g) Fe SAs/HOPSNC; WT-EXAFS plots of Ni K-edge EXAFS for (h) FeNi DASs/HOPSNC and (i) Ni SAs/HOPSNC.

experimental spectra, and the average diatomic bond length in good agreement with the distance between the dual dots observed in the STEM measurements (Figs. 4e and S12). The model presented in Fig. 4e inset shows the best fitting results and an average of four N-coordinated with either Fe or Ni, indicating the formation of 2 N-bridged (Fe-Ni)N$_6$. The detailed fitting parameters are summarized in Table S2. It should be noted that Fe, Ni and even residual Zn can also be inevitably involved in the diatomic sites during pyrolysis, leading to other possible atomic pairs such as Fe-Fe, Ni-Ni, Fe-Zn, Ni-Zn and/or Zn-Zn. To identify the M-N bonds, the wavelet transform (WT) of the EXAFS spectra was also performed (Fig. 4f-i). In the WT-EXAFS plots, Ni SAs/HOPSNC and FeNi DASs/HOPSNC show the same maximum intensity at 3.9 Å^{-1} for the Ni-N path in the Ni K-edge reference, while Fe SAs/HOPSNC and FeNi DASs/HOPSNC also display the same maximum intensity at 3.8 Å^{-1} for the Fe-N path in the Fe K-edge reference. The (Fe-Ni)N$_6$ diatomic co-ordination configuration with relatively strong coupling interaction would result in asymmetric charge distribution, which could be favorable to the activation of the reactants and thus prompt the electro-catalytic properties.

3.2. Electrocatalytic performance for CO$_2$RR

In view of the unique spatial superstructure and atomic pair structure of FeNi DASs/HOPSNC, the electrocatalytic performance for CO$_2$RR was evaluated in a standard three-electrode system using 0.5 M KHCO$_3$ solution saturated with CO$_2$ as the electrolyte in an H-type cell. For comparison, the single-metal catalysts Fe SAs/HOPSNC and Ni SAs/

HOPSNC were also studied. By systematically controlling the concentration of Fe and Ni in OM-Fe/Ni-ZIF-8 and the mass ratio of DCDA to OM-Fe/Ni-ZIF-8 during catalyst preparation, the FeNi DASs/HOPSNC catalyst with an optimized electrochemical performance was identified (Figs. S14 and S15). As evaluated by the linear sweep voltammetric (LSV) curves in Fig. 5a, Fe SAs/HOPSNC and Ni SAs/HOPSNC exhibits the lowest and highest onset potentials for CO$_2$RR, respectively, due to their different barriers for the formation of *COOH intermediate. Remarkably, FeNi DASs/HOPSNC possessing a moderate onset potential is capable of offering the highest total current density for CO$_2$RR. The gas and liquid products were quantified by online gas chromatography (GC) and nuclear magnetic resonance (NMR), which indicated that CO and H$_2$ were the exclusive products and no liquid products were detected (Fig. S17). The CO partial current densities (j_{CO}) were compared at various applied potentials, as shown in Fig. 5b. To be specific, FeNi DASs/HOPSNC delivered a superior j_{CO} (50.2 mA cm^{-2} at −1.08 V vs. RHE), greatly outperforming Fe SAs/HOPSNC (12.5 mA cm^{-2}) and Ni SAs/HOPSNC (38.6 mA cm^{-2}). Meanwhile, FeNi DASs/HOPSNC presents high FE$_{CO}$ over 90% in the large potential window from − 0.68 to − 1.08 V (Fig. 5c). Impressively, FeNi DASs/HOPSNC exhibited an excellent stability for CO$_2$RR, retaining nearly unchanged current density of 37 mA cm^{-2} and FE$_{CO}$ above 90% over 9 h continuous electrolysis at − 0.87 V (Fig. 5d). Besides, the structure and morphology of the electrocatalyst were well preserved after the stability test (Fig. S18). Contrastively, Ni SAs/HOPSNC show the much inferior stability with significantly reduced selectivity (Fig. S19). Worse still, Fe SAs/HOPSNC exhibited even sharper decline in FE$_{CO}$ and current
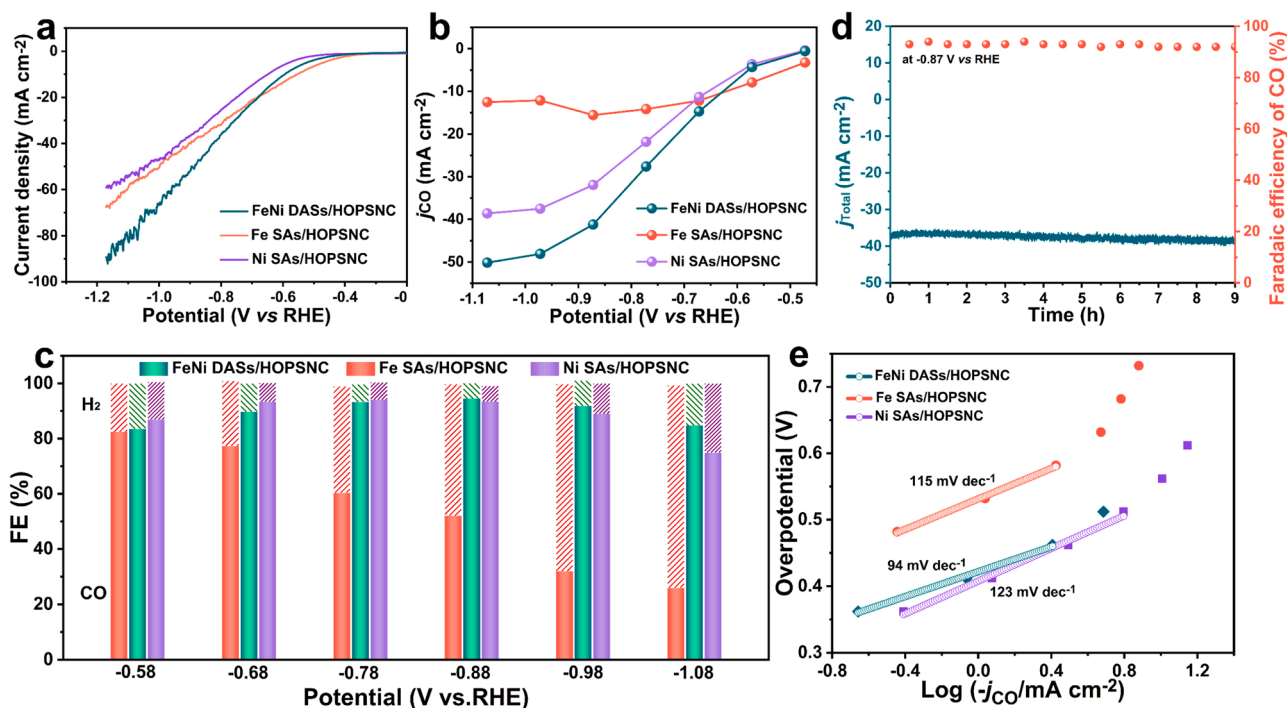
Fig. 5. Electrocatalytic CO_2RR performances of FeNi DASs/HOPSNC, Fe SAs/HOPSNC and Ni SAs/HOPSNC: (a) LSV curves; (b) j_{CO} and (c) FE_{CO} at different potentials; (d) stability test for FeNi DASs/HOPSNC; (e) Tafel slope diagrams.

density with dominant H_2 product (Fig. S20), which could be due to the fact that the strong binding of the Fe SA sites and reaction intermediate *CO seriously compromises FE and stability during the stability test. Moreover, the kinetic performance of the CO_2RR was then assessed by the Tafel analysis. As shown in Fig. 5e, the Tafel slope for CO generation over FeNi DASs/HOPSNC was surveyed to be 94 mV dec^{-1}, much lower than those of Fe SAs/HOPSNC (115 mV dec^{-1}) and Ni SAs/HOPSNC (123 mV dec^{-1}), indicating that the first electron transfer is the rate-determining step for CO_2RR and the Fe-Ni diatomic pair configuration is conducive to promote the formation of the *COOH intermediate. These results demonstrate that the synergetic effect of Fe-Ni atomic pair configurations in the electrocatalysts optimizes the electronic structures and the corresponding interactions between active sites and intermediates, thus obviously improving the intrinsic activity and stability.

FeNi DASs/HOPSNC can obtain high j_{CO} and FE_{CO} at the same time in the H-type cell, showing a good application prospect. However, the low solubility of CO_2 in aqueous electrolytes severely limits the current density of CO_2RR in the H-type cell, making it difficult to approach the large current density values (>200 mA cm^{-2}). Therefore, a gas diffusion electrode (GDE) loaded with the FeNi DASs/HOPSNC catalyst was further constructed with a three-phase interface between gaseous CO_2, solid catalyst, and aqueous electrolyte (Figs. 6a and S22). As shown in Fig. 6b, the current density for CO_2RR over FeNi DASs/HOPSNC in the GDE-based flow cell was significantly improved, due to the boosted CO_2 diffuse, where an ultralow onset potential of ca. − 0.12 V vs RHE and high current density up to 370 mA cm^{-2} were achieved. Meanwhile, FeNi DASs/HOPSNC can deliver stable current densities at different applied potentials, and the FE_{CO} remained nearly 100% across a broad potential range of − 0.37 to − 1.37 V (Fig. 6c and d). It is worth noting that FeNi DASs/HOPSNC afforded an outstanding partial CO current density of 300 mA cm^{-2} at − 1.37 V vs RHE. In addition, an impressive stability of the catalyst with the nearly 100% FE_{CO} maintenance in this flow cell was displayed during the continuous electrolysis at a current density of 200 mA cm^{-2} (Fig. 6e). Notably, in terms of electrocatalytic activity and selectivity, FeNi DASs/HOPSNC surpasses most of reported

metal atomic electrocatalysts (Fig. 6f and Table S4). Consequently, the exceptional catalytic performance makes FeNi DASs/HOPSNC promising to be applied for the practical CO_2RR electrolysis.

3.3. Mechanistic study

DFT calculations were employed to further explore the mechanism of the electrocatalytic CO_2RR process over FeNi DASs/HOPSNC. The structural configuration of the Fe-Ni atomic pair site applied for theoretical study is 2 N-bridged $(Fe-Ni)N_6$, as indicated by the XAS results. For comparison, we also constructed the $Fe-N_4$ models for Fe SAs/HOPSNC and $Ni-N_4$ models for Ni SAs/HOPSNC. Meanwhile, the Fe_2N_6 and Ni_2N_6 models were also displayed for the integrity. According to previous studies, the intermediates are adsorbed with both Fe and Ni atoms in FeNi DASs/HOPSNC [35]. As illustrated in Fig. 7a and S25, Gibbs free energy diagrams for the pathways were calculated to elucidate the intrinsic mechanism of CO_2RR process. Obviously, FeNi DASs/HOPSNC with the Fe-Ni atomic pair sites exhibits a comparable energy barrier for *COOH formation to Fe SAs/HOPSNC, but much lower than that of Ni SAs/HOPSNC, which indicates that the CO_2RR is more readily to occur on FeNi DASs/HOPSNC and Fe SAs/HOPSNC, consistent with their smaller initial potentials. Moreover, compared to the single-atom Fe sites of Fe SAs/HOPSNC, the slightly weaker binding energy of *CO on the Fe-Ni diatomic sites could facilitate the desorption of CO over FeNi DASs/HOPSNC, thus avoiding the CO poisoning and promoting the catalytic process. In addition, the Gibbs free energy values of Fe-Fe, Ni-Ni and Fe-Ni diatomic sites were also compared. The Ni-Ni diatomic sites display a highest energy barrier for *COOH, and the Fe-Fe diatomic sites are difficult to facilitate the desorption of CO. Therefore, compared with the Fe-Fe and Ni-Ni diatomic sites, the Fe-Ni diatomic sites are more favorable for CO_2-to-CO (Fig. S23). The HER is considered as a competitive reaction against the CO_2RR, thus the differences between the thermodynamic limiting potentials for CO_2RR and HER (denoted as $U_{L(CO2)}$ - $U_{L(H2)}$ ($U_L = -\Delta G_0/e$)) are considered to evaluate the selectivity during electroreduction. As illustrated in Fig. 7b, Fe SAs/HOPSNC shows the most negative difference value, indicating its
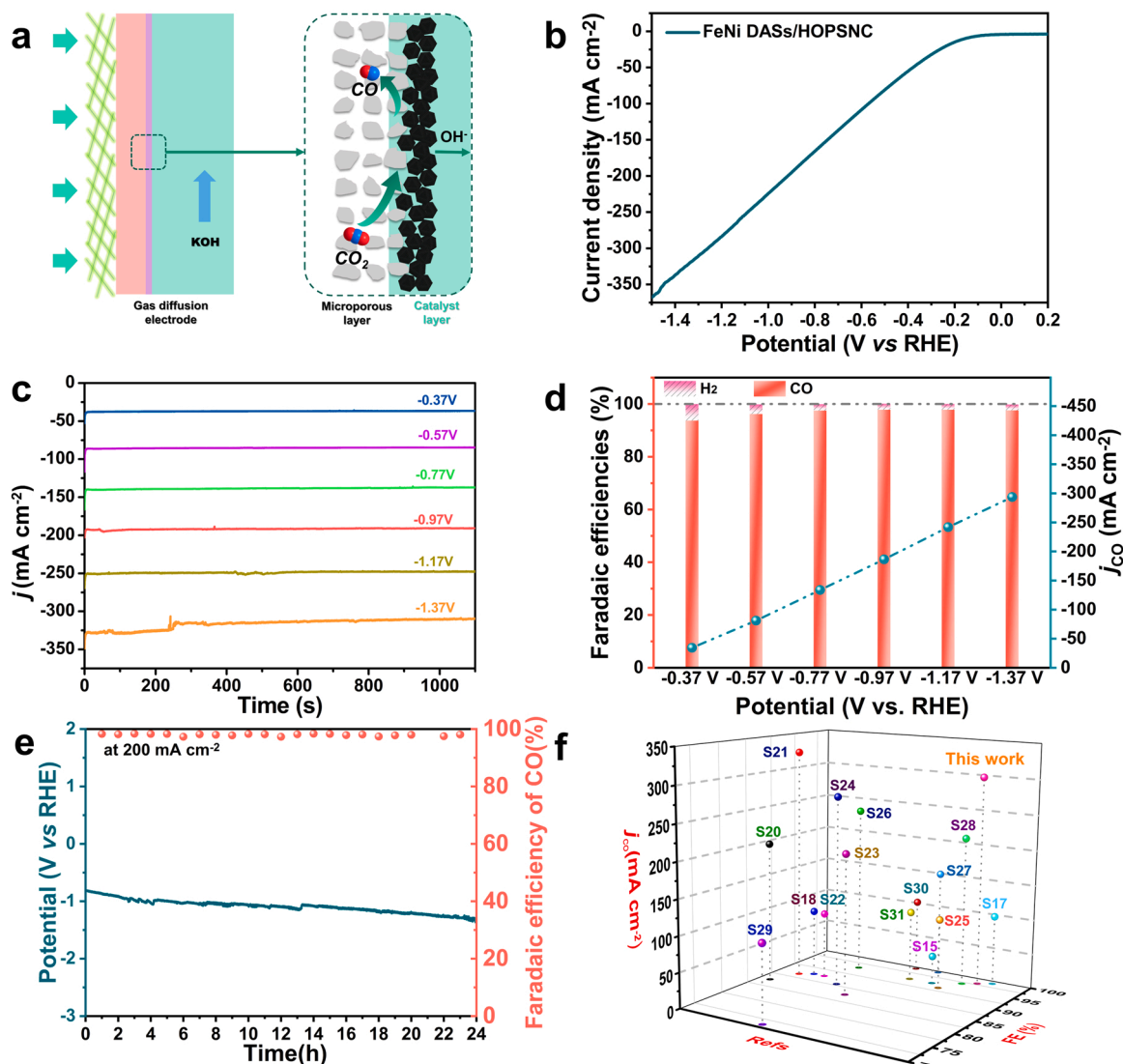
Fig. 6. (a) Schematic illustration of a flow cell configuration; (b) LSV curves of FeNi DASs/HOPSNC in the flow cell; (c) i-t curves for CO_2RR; (d) CO Faradaic efficiency diagram; (e) current density diagram for catalytic reduction of carbon dioxide at 200 mA cm^{-2}; (f) comparison of j_{CO} and FE for FeNi DASs/HOPSNC at − 1.37 V and recently reported catalysts.

poor selectivity toward CO_2RR. However, after pairing with Ni atoms, FeNi DASs/HOPSNC exhibits a much positive difference value comparable to Ni SAs/HOPSNC, resulting in an excellent CO selectivity [46]. Further, the charge density differences of the intermediates *COOH, *CO and *H on FeNi DASs/HOPSNC, Fe SAs/HOPSNC and Ni SAs/HOPSNC were calculated (Figs. 7c and S24). It is easy to find that more electrons are localized around Ni-Fe atoms in FeNi DASs/HOPSNC, which indicates the Fe-Ni diatomic sites transfer less electrons to the adjacent N atoms and show the lower oxidation states than those of the isolated Fe and Ni atoms in Fe SAs/HOPSNC and Ni SAs/HOPSNC, respectively. Bader charge analysis further revealed the much lower oxidation states of the Fe-Ni active sites combined with the intermediates *COOH, *CO and *H (Fig. 7c), which promotes the formation of *COOH and the desorption of *CO on FeNi DASs/HOPSNC. Furthermore, the projected density of states (PDOS) uncovers the interaction between *COOH and the metal atoms (Fig. 7d). The D-band center of the Ni atom upshifts significantly from −2.66 to −1.18 eV with the introduction of the Fe atom, which is favorable for facilitating transfer of electrons and accelerating the formation of *COOH during the CO_2RR process. Therefore, the DFT calculations unveil that the Fe-Ni atomic pair sites with the modulated electronic structure could promote

the intrinsic activity and selectivity of the active sties toward CO_2RR and thus boost the overall CO_2RR catalytic performance, which is in well agreement with the experimental results.

4. Conclusion

In summary, a hierarchically ordered porous superstructure of N-doped carbon embedded with readily accessible Fe-Ni atomic pair sites has been constructed using the ordered macroporous MOF single-crystals as the self-template. The integrated highly ordered macroporous and mesoporous structure of the as-synthesized FeNi DASs/HOPSNC ensures the efficient mass transport and the accessibility of the highly exposed Fe-Ni atomic pair sites. Meanwhile, the synergistic interactions of the adjacent Fe-Ni atoms promotes *COOH formation and *CO desorption while inhibiting the HER, as interpreted by the systematic contrast experiments and DFT calculations, which greatly improves the intrinsic activity and selectivity of the catalyst. As a joint result, both the kinetic and thermodynamic properties of FeNi DASs/HOPSNC are significantly promoted, delivering an exceptional electrocatalytic performance for CO_2RR with large current density up to 300 mA cm^{-2}, near-unity FE_{CO} in a wide potential range and satisfied
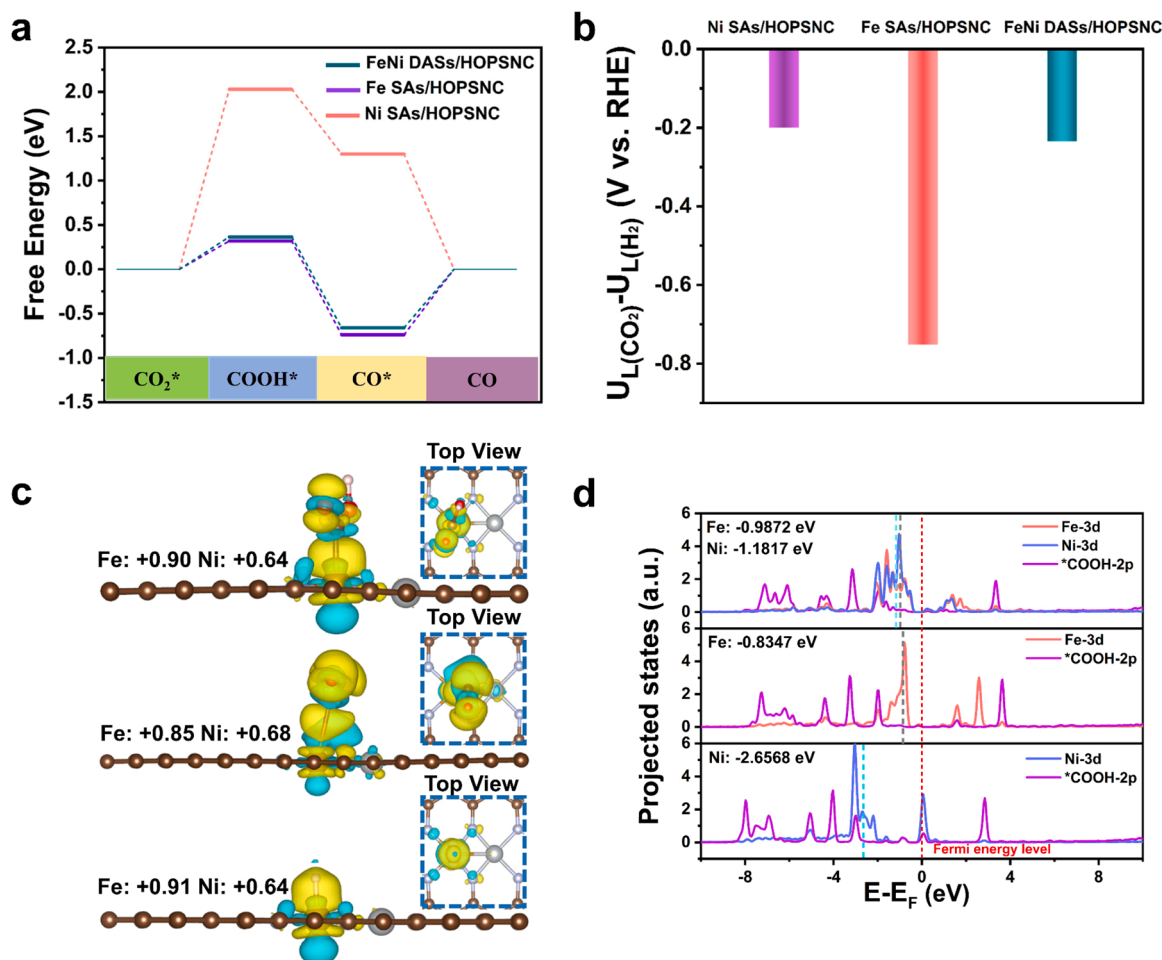
Fig. 7. Calculation for FeNi DASs/HOPSNC, Fe SAs/HOPSNC and Ni SAs/HOPSNC: (a) Gibbs free energy diagram of CO_2RR process; (b) the differences in limiting potentials for CO_2RR ($U_{L(CO_2)}$) and HER ($U_{L(H_2)}$) over the active sites; (c) Charge density difference and Bader charge analysis of the intermediates *COOH, *CO and *H on the active sites. Yellow and blue represent electron accumulation and depletion, respectively; (d) projected density of states (PDOS) for Fe/Ni 3d orbitals and oxide 2p orbitals of the active sites.

stability. This work gives an important reference on the design and preparation of advanced electrocatalysts with both desired spatial structure and atomic site structure for CO_2 reduction and other electrochemical techniques.

CRediT authorship contribution statement

Lei Jiao, Qiang Xu and **Qi-Long Zhu** conceived the research and designed the experiments. **Lei Jiao** and **Xiaofang Li** carried out the synthesis, material characterizations and electrochemical measurements. **Shu-Guo Han, Wenbo Wei, Sheng-Hua Zhou, Yue Mao, Xin-Tao Wu** and **Qi-Long Zhu** analysed the data. **Lei Jiao, Xiaofang Li, Qiang Xu** and **Qi-Long Zhu** drafted the manuscript. All authors discussed and revised the manuscript.

Declaration of Competing Interest

The authors declare that they have no known competing financial interests or personal relationships that could have appeared to influence the work reported in this paper.

Data availability

Data will be made available on request.

Appendix A. Supplementary material

Supplementary data associated with this article can be found in the online version at doi:10.1016/j.apcatb.2023.122638.

References

[1] M.B. Ross, P. De Luna, Y. Li, C.-T. Dinh, D. Kim, P. Yang, E.H. Sargent, Designing materials for electrochemical carbon dioxide recycling, Nat. Catal. 2 (2019) 648–658, https://doi.org/10.1038/s41929-019-0306-7.

[2] D.D. Zhu, J.L. Liu, S.Z. Qiao, Recent advances in inorganic heterogeneous electrocatalysts for reduction of carbon dioxide, Adv. Mater. 28 (2016) 3423–3452, https://doi.org/10.1002/adma.201504766.

[3] J.Y.T. Kim, P. Zhu, F.-Y. Chen, Z.-Y. Wu, D.A. Cullen, H. Wang, Recovering carbon losses in CO_2 electrolysis using a solid electrolyte reactor, Nat. Catal. 5 (2022) 288–299, https://doi.org/10.1038/s41929-022-00763-w.

[4] Q. He, J.H. Lee, D. Liu, Y. Liu, Z. Lin, Z. Xie, S. Hwang, S. Kattel, L. Song, J.G. Chen, Accelerating CO_2 electroreduction to CO over Pd single-atom catalyst, Adv. Funct. Mater. 30 (2020), 2000407, https://doi.org/10.1002/adfm.202000407.

[5] S.-G. Han, M. Zhang, Z.-H. Fu, L. Zheng, D.-D. Ma, X.-T. Wu, Q.-L. Zhu, Enzyme-inspired microenvironment engineering of a single-molecular heterojunction for promoting concerted electrochemical CO_2 reduction, Adv. Mater. (2022), 2202830, https://doi.org/10.1002/adma.202202830.

[6] D.-D. Ma, S.-G. Han, C. Cao, W. Wei, X. Li, B. Chen, X.-T. Wu, Q.-L. Zhu, Bifunctional single-molecular heterojunction enables completely selective CO_2-to-CO conversion integrated with oxidative 3D nano-polymerization, Energy Environ. Sci. 14 (2021) 1544–1552, https://doi.org/10.1039/d0ee03731a.

[7] M.-K. Hu, S.-H. Zhou, D.-D. Ma, Q.-L. Zhu, New insight into heterointerfacial effect for heterogenized metallomacrocycle catalysts in executing electrocatalytic CO_2 reduction, Appl. Catal. B Environ. 310 (2022), 121324, https://doi.org/10.1016/j.apcatb.2022.121324.

[8] Q. Lu, J. Rosen, Y. Zhou, G.S. Hutchings, Y.C. Kimmel, J.G. Chen, F. Jiao, A selective and efficient electrocatalyst for carbon dioxide reduction, Nat. Commun. 5 (2014) 3242, https://doi.org/10.1038/ncomms4242.

[9] W. Zhu, Y.-J. Zhang, H. Zhang, H. Lv, Q. Li, R. Michalsky, A.A. Peterson, S. Sun, Active and selective conversion of CO_2 to CO on ultrathin Au nanowires, J. Am. Chem. Soc. 136 (2014) 16132–16135, https://doi.org/10.1021/ja5095099.

[10] B.A. Rosen, A. Salehi-Khojin, M.R. Thorson, W. Zhu, D.T. Whipple, P.J.A. Kenis, R. I. Masel, Ionic liquid-mediated selective conversion of CO_2 to CO at low overpotentials, Science 334 (2011) 643–644, https://doi.org/10.1126/science.1209786.

[11] S. Chen, X. Li, C.-W. Kao, T. Luo, K. Chen, J. Fu, C. Ma, H. Li, M. Li, T.-S. Chan, M. Liu, Unveiling the proton-feeding effect in sulfur-doped Fe-N-C single-atom catalyst for enhanced CO_2 electroreduction, Angew. Chem. Int. Ed. 61 (2022), e202206233, https://doi.org/10.1002/anie.202206233.

[12] X. Sun, Y. Tuo, C. Ye, C. Chen, Q. Lu, G. Li, P. Jiang, S. Chen, P. Zhu, M. Ma, J. Zhang, J.H. Bitter, D. Wang, Y. Li, Phosphorus induced electron localization of single iron sites for boosted CO_2 electroreduction reaction, Angew. Chem. Int. Ed. 60 (2021) 23614–23618, https://doi.org/10.1002/anie.202110433.

[13] S. Chen, X. Li, C.-W. Kao, T. Luo, K. Chen, J. Fu, C. Ma, H. Li, M. Li, T.-S. Chan, M. Liu, Unveiling the proton-feeding effect in sulfur-doped Fe-N-C single-atom catalyst for enhanced CO_2 electroreduction, Angew. Chem. Int. Ed. 61 (2022), https://doi.org/10.1002/anie.202206233.

[14] M. Liu, X. Liu, D. Fu, Z. Xie, X. Zou, W. Liu, Y. Yu, J. Wang, H. Wang, C. Tong, Z. Cheng, S. Wu, K. Ding, Y. Yu, A facile complexing agent-assistant single atom Ag-N_3S_1 site photodeposition strategy, Appl. Catal. B Environ. 318 (2022), 121896, https://doi.org/10.1016/j.apcatb.2022.121896.

[15] X. Cui, W. Li, P. Ryabchuk, K. Junge, M. Beller, Bridging homogeneous and heterogeneous catalysis by heterogenized single-metal-site catalysts, Nat. Catal. 1 (2018) 385–397, https://doi.org/10.1038/s41929-018-0090-9.

[16] A. Wang, J. Li, T. Zhang, Heterogeneous single-atom catalysis, Nat. Rev. Chem. 2 (2018) 65–81, https://doi.org/10.1038/s41570-018-0010-1.

[17] B. Qiao, A. Wang, X. Yang, L.F. Allard, Z. Jiang, Y. Cui, J. Liu, J. Li, T. Zhang, Single-atom catalysis of CO oxidation using Pt-1/FeOx, Nat. Chem. 3 (2011) 634–641, https://doi.org/10.1038/nchem.1095.

[18] L. Liu, A. Corma, Metal catalysts for heterogeneous catalysis: from single atoms to nanoclusters and nanoparticles, Chem. Rev. 118 (2018) 4981–5079, https://doi.org/10.1021/acs.chemrev.7b00776.

[19] W. Wang, Y. Chao, W. Zhang, J. Zhou, F. Lv, K. Wang, F. Lin, H. Luo, J. Li, M. Tong, E. Wang, S. Guo, Emerging dual-atomic-site catalysts for efficient energy catalysis, Adv. Mater. 33 (2021), 2102576, https://doi.org/10.1002/adma.202102576.

[20] A.S. Varela, N.R. Sahraie, J. Steinberg, W. Ju, H.-S. Oh, P. Strasser, Metal-doped nitrogenated carbon as an efficient catalyst for direct CO_2 electroreduction to CO and hydrocarbons, Angew. Chem. Int. Ed. 54 (2015) 10758–10762, https://doi.org/10.1002/ange.201502099.

[21] W. Ju, A. Bagger, G.-P. Hao, A.S. Varela, I. Sinev, V. Bon, B.R. Cuenya, S. Kaskel, J. S. Rossmeisl, Peter, Understanding activity and selectivity of metal-nitrogen-doped carbon catalysts for electrochemical reduction of CO_2, Nat. Commun. 8 (2017) 944, https://doi.org/10.1038/s41467-017-01035-z.

[22] Y. Li, S.L. Zhang, W. Cheng, Y. Chen, D. Luan, S. Gao, X.W. Lou, Loading single-Ni atoms on assembled hollow N-rich carbon plates for efficient CO_2 electroreduction, Adv. Mater. 34 (2022), 2105204, https://doi.org/10.1002/adma.202105204.

[23] T. Zheng, K. Jiang, N. Ta, Y. Hu, J. Zeng, J. Liu, H. Wang, Large-scale and highly selective CO_2 electrocatalytic reduction on nickel single-atom catalyst, Joule 3 (2019) 265–278, https://doi.org/10.1016/j.joule.2018.10.015.

[24] H. Guo, D.-H. Si, H.-J. Zhu, Q.-X. Li, Y.-B. Huang, R. Cao, Ni single-atom sites supported on carbon aerogel for highly efficient electroreduction of carbon dioxide with industrial current densities, eScience 2 (2022) 295–303, https://doi.org/10.1016/j.esci.2022.03.007.

[25] T. Moeller, W. Ju, A. Bagger, X. Wang, F. Luo, T. Trung Ngo, A.S. Varela, J. Rossmeisl, P. Strasser, Efficient CO_2 to CO electrolysis on solid Ni-N-C catalysts at industrial current densities, Energy Environ. Sci. 12 (2019) 640–647, https://doi.org/10.1039/C8EE02662A.

[26] J. Gu, C.-S. Hsu, L. Bai, H.M. Chen, X. Hu, Atomically dispersed Fe^{3+} sites catalyze efficient CO_2 electroreduction to CO, Science 364 (2019) 1091–1094, https://doi.org/10.1126/science.aaw7515.

[27] F. Pan, B. Li, E. Sarnello, Y. Fei, Y. Gang, X. Xiang, Z. Du, P. Zhang, G. Wang, H. T. Nguyen, T. Li, Y.H. Hu, H.-C. Zhou, Y. Li, Atomically dispersed iron-nitrogen sites on hierarchically mesoporous carbon nanotube and graphene nanoribbon networks for CO_2 reduction, ACS Nano 14 (2020) 5506–5516, https://doi.org/10.1021/acsnano.9b09658.

[28] Y.-N. Gong, L. Jiao, Y. Qian, C.-Y. Pan, L. Zheng, X. Cai, B. Liu, S.-H. Yu, H.-L. Jiang, Regulating the coordination environment of MOF-templated single-atom nickel electrocatalysts for boosting CO_2 reduction, Angew. Chem. Int. Ed. 59 (2020) 2705–2709, https://doi.org/10.1002/ange.201914977.

[29] J. Leverett, R. Daiyan, L. Gong, K. Iputera, Z. Tong, J. Qu, Z. Ma, Q. Zhang, S. Cheong, J. Cairney, R.-S. Liu, X. Lu, Z. Xia, L. Dai, R. Amal, Designing undercoordinated Ni-N_x and Fe-N_x on holey graphene for electrochemical CO_2 conversion to syngas, ACS Nano 15 (2021) 12006–12018, https://doi.org/10.1021/acsnano.1c03293.

[30] Z. Jin, P. Li, Y. Meng, Z. Fang, D. Xiao, G. Yu, Understanding the inter-site distance effect in single-atom catalysts for oxygen electroreduction, Nat. Catal. 4 (2021) 615–622, https://doi.org/10.1038/s41929-021-00650-w.

[31] B. Wang, C. Cheng, M. Jin, J. He, H. Zhang, W. Ren, J. Li, D. Wang, Y. Li, A site distance effect induced by reactant molecule matchup in single-atom catalysts for fenton-like reactions, e202207268-e202207268, Angew. Chem. Int. Ed. 134 (2022), https://doi.org/10.1002/anie.202207268.

[32] J. Song, Z. Chen, X. Cai, X. Zhou, G. Zhan, R. Li, P. Wei, N. Yan, S. Xi, Kp Loh, Promoting dinuclear-type catalysis in Cu_1-C_3N_4 single atom catalyst, Adv. Mater. 34 (2022), 2204638, https://doi.org/10.1002/adma.202204638.

[33] B. Wulan, X. Cao, D. Tan, X. Shu, J. Zhang, Atomic bridging of metal-nitrogen-carbon toward efficient integrated electrocatalysis, Adv. Funct. Mater. 32 (2022), 2203842, https://doi.org/10.1002/adfm.202203842.

[34] Y. Li, B. Wei, M. Zhu, J. Chen, Q. Jiang, B. Yang, Y. Hou, L. Lei, Z. Li, R. Zhang, Y. Lu, Synergistic effect of atomically dispersed Ni-Zn pair sites for enhanced CO_2 electroreduction, Adv. Mater. 33 (2021), 2102212, https://doi.org/10.1002/adma.202102212.

[35] W. Ren, X. Tan, W. Yang, C. Jia, S. Xu, K. Wang, S.C. Smith, C. Zhao, Isolated diatomic Ni-Fe metal-nitrogen sites for synergistic electroreduction of CO_2, Angew. Chem. Int. Ed. 58 (2019) 6972–6976, https://doi.org/10.1002/anie.201901575.

[36] J. Zhu, M. Xiao, D. Ren, R. Gao, X. Liu, Z. Zhang, D. Luo, W. Xing, D. Su, A. Yu, Z. Chen, Quasi-covalently coupled Ni-Cu atomic pair for synergistic electroreduction of CO_2, J. Am. Chem. Soc. 144 (2022) 9661–9671, https://doi.org/10.1021/jacs.2c00937.

[37] X. Wan, X. Liu, Y. Li, R. Yu, L. Zheng, W. Yan, H. Wang, M. Xu, J. Shui, Fe-N-C electrocatalyst with dense active sites and efficient mass transport for high-performance proton exchange membrane fuel cells, Nat. Catal. 2 (2019) 259–268, https://doi.org/10.1038/s41929-019-0237-3.

[38] L. Shang, H. Yu, X. Huang, T. Bian, R. Shi, Y. Zhao, G.I.N. Waterhouse, L.-Z. Wu, C.-H. Tung, T. Zhang, Well-dispersed ZIF-derived Co,N-co-doped carbon nanoframes through mesoporous-silica-protected calcination as efficient oxygen reduction electrocatalysts, Adv. Mater. 28 (2016) 1668–1674, https://doi.org/10.1002/adma.201505045.

[39] Z. Zhu, H. Yin, Y. Wang, C.-H. Chuang, L. Xing, M. Dong, Y.-R. Lu, G. Casillas-Garcia, Y. Zheng, S. Chen, Y. Dou, P. Liu, Q. Cheng, H. Zhao, Coexisting single-atomic Fe and Ni sites on hierarchically ordered porous carbon as a highly efficient ORR electrocatalyst, Adv. Mater. 32 (2020), 2004670, https://doi.org/10.1002/adma.202004670.

[40] L. Jiao, J. Zhu, Y. Zhang, W. Yang, S. Zhou, A. Li, C. Xie, X. Zheng, W. Zhou, S.-H. Yu, H.-L. Jiang, Non-bonding interaction of neighboring Fe and Ni single-atom pairs on MOF-derived N-doped carbon for enhanced CO_2 electroreduction, J. Am. Chem. Soc. 143 (2021) 19417–19424, https://doi.org/10.1021/jacs.1c08050.

[41] Y. Zhang, L. Jiao, W. Yang, C. Xie, H.-L. Jiang, Rational fabrication of low-coordinate single-atom Ni electrocatalysts by MOFs for highly selective CO_2 reduction, Angew. Chem. Int. Ed. 60 (2021) 7607–7611, https://doi.org/10.1002/anie.202016219.

[42] X. Li, Q.-L. Zhu, MOF-based materials for photo- and electrocatalytic CO_2 reduction, EnergyChem 2 (2020), 100033, https://doi.org/10.1016/j.enchem.2020.100033.

[43] H. Zhou, T. Yang, Z. Kou, L. Shen, Y. Zhao, Z. Wang, X. Wang, Z. Yang, J. Du, J. Xu, M. Chen, L. Tian, W. Guo, Q. Wang, H. Lv, W. Chen, X. Hong, J. Luo, D. He, Y. Wu, Negative pressure pyrolysis induced highly accessible single sites dispersed on 3D graphene frameworks for enhanced oxygen reduction, Angew. Chem. Int. Ed. 59 (2020) 20465–20469, https://doi.org/10.1002/anie.202009700.

[44] J. Pampel, T.-P. Fellinger, Opening of bottleneck pores for the improvement of nitrogen doped carbon electrocatalysts, Adv. Energy Mater. 6 (2016), 1502389, https://doi.org/10.1002/aenm.201502389.

[45] M.K. Albolkany, C. Liu, Y. Wang, C.-H. Chen, C. Zhu, X. Chen, B. Liu, Molecular surgery at microporous MOF for mesopore generation and renovation, Angew. Chem. Int. Ed. 60 (2021) 14601–14608, https://doi.org/10.1002/ange.202103104.

[46] X. Chen, D.-D. Ma, B. Chen, K. Zhang, R. Zou, X.-T. Wu, Q.-L. Zhu, Metal-organic framework-derived mesoporous carbon nanoframes embedded with atomically dispersed Fe-N_x active sites for efficient bifunctional oxygen and carbon dioxide electroreduction, Appl. Catal. B Environ. 267 (2020), 118720, https://doi.org/10.1016/j.apcatb.2020.118720.

[47] J. Ding, Z. Liu, X. Liu, B. Liu, J. Liu, Y. Deng, X. Han, W. Hu, C. Zhong, Tunable periodically ordered mesoporosity in palladium membranes enables exceptional enhancement of intrinsic electrocatalytic activity for formic acid oxidation, Angew. Chem. Int. Ed. 59 (2020) 5092–5101, https://doi.org/10.1002/ange.201914649.

[48] K. Shen, L. Zhang, X. Chen, L. Liu, D. Zhang, Y. Han, J. Chen, J. Long, R. Luque, Y. Li, B. Chen, Ordered macro-microporous metal-organic framework single crystals, Science 359 (2018) 206–210, https://doi.org/10.1126/science.aao3403.

[49] F. Wang, T. Hou, X. Zhao, W. Yao, R. Fang, K. Shen, Y. Li, Ordered macroporous carbonous frameworks implanted with CdS quantum dots for efficient photocatalytic CO_2 reduction, Adv. Mater. 33 (2021), 2102690, https://doi.org/10.1002/adma.202102690.

[50] N. Wang, X. Li, M.-K. Hu, W. Wei, S.-H. Zhou, X.-T. Wu, Q.-L. Zhu, Ordered macroporous superstructure of bifunctional cobalt phosphide with heteroatomic modification for paired hydrogen production and polyethylene terephthalate plastic recycling, Appl. Catal. B Environ. 316 (2022), 121667, https://doi.org/10.1016/j.apcatb.2022.121667.

[51] S. Shen, C. Han, B. Wang, Y. Wang, Engineering d-band center of nickel in nickel@ nitrogen-doped carbon nanotubes array for electrochemical reduction of CO_2 to CO and $Zn-CO_2$ batteries, Chin. Chem. Lett. 33 (2022) 3721–3725, https://doi.org/10.1016/j.cclet.2021.10.063.

[52] Y. Li, W. Shan, M.J. Zachman, M. Wang, S. Hwang, H. Tabassum, J. Yang, X. Yang, S. Karakalos, Z. Feng, G. Wang, G. Wu, Atomically dispersed dual-metal site catalysts for enhanced CO_2 reduction: mechanistic insight into active site structures, Angew. Chem. Int. Ed. 61 (2022), e202205632, https://doi.org/10.1002/anie.202205632.